

Atomic Arrangements of AuPt/Pt(111) and AuPd/Pd(111) Surface Alloys: A Combined Density Functional Theory and Monte Carlo Study

J. Adam Stephens, Hyung Chul Ham, and Gyeong S. Hwang*

Department of Chemical Engineering, The University of Texas at Austin, Austin, Texas 78712, United States

Received: August 7, 2010; Revised Manuscript Received: October 6, 2010

We have constructed model Hamiltonians for AuPt/Pt(111) and AuPd/Pd(111) surface alloys based on the cluster expansion method and density functional theory. Using these cluster expansions in Monte Carlo simulations, we have calculated the size and shape distributions of Pt and Pd ensembles in these two materials for a range of compositions and temperatures. We report on and explain the results of our simulations in terms of the differing interatomic interactions present in each alloy. Through the use of electronic structure calculations, we find that in AuPt, homonuclear Pt–Pt interactions are favored over heteronuclear Au–Pt interactions, while in AuPd the opposite is true. Accordingly, our simulations show that Pd prefers to form small, isolated ensembles with extended shapes, and Pt prefers to agglomerate and form larger ensembles with compact shapes.

I. Introduction

Bimetallic alloys frequently exhibit greatly enhanced catalytic properties compared to their monometallic constituents.^{1–3} There is increasing interest in understanding the catalytic effects of alloying pure gold with other metals.^{4,5} Alloying gold (Au) with palladium (Pd) or platinum (Pt) has been shown to result in a bimetallic catalyst having superior activity and selectivity toward various catalytic reactions.^{6–10} In addition, alloying has been shown to increase the stability of Au particles against sintering.¹¹ While the underlying mechanism for the alloying effect is not fully understood, it has been thought that the improved catalytic function of bimetallics could be attributed to modifications of the electronic structure by metal–metal interactions [the so-called ligand (electronic) effect] and unique mixed-metal surface sites [the ensemble (geometric) effect].^{12–14}

In particular, the importance of specific ensembles, or arrangements of atoms, in the surface layer has been evidenced by a series of recent studies. Baddeley et al.¹⁵ found evidence that ensembles containing 6 or 7 Pd atoms are active for the formation of benzene from acetylene on AuPd(111) surfaces. Kumar et al.⁴ identified second nearest neighbor pairs of Pd monomers in the AuPd(100) alloy as a particularly active ensemble for vinyl acetate synthesis. In the AuPd(111) alloy, a recent first principles study^{16,17} demonstrated that the selectivity of H₂O₂ in direct oxidation of H₂ is a strong function of the arrangement of Pd and Au surface atoms. In particular, isolated Pd monomers surrounded by less active Au atoms are primarily responsible for the significantly enhanced H₂O₂ selectivity by suppressing O–O bond cleavage. It has also been reported that Pd monomers play a significant role in enhancing the catalytic activity for hydrogen evolution^{10,18} and carbon monoxide adsorption and oxidation.^{19–21}

The close identification between catalytic function and specific surface ensembles suggests the importance of understanding ensemble formation in alloyed surfaces. Although direct characterization of surface atomic arrangements has been limited, computational approaches can be a powerful and flexible

alternative. Boscoboinik et al. recently developed a model based on first neighbor pair interactions in AuPd (111) surface alloys that they used to examine the distributions of Pd ensembles²² and to count specific adsorption sites.²³ On the basis of scanning tunneling microscope (STM) images of AuPt(111) surface alloys, Bergbeiter et al.²⁴ derived effective pair interaction parameters that they used in Monte Carlo simulations to calculate ensemble populations. These studies demonstrate the usefulness of simulation tools in this area and also indicate the importance of the interactions between surface layer atoms in ensemble formation. However, the nature and consequences of interatomic interactions in surface alloys are still not fully understood.

In this paper, we present a simulation scheme to predict the equilibrium size and shape distributions of surface ensembles in AuPd/Pd(111) and AuPt/Pt(111) alloys at a range of temperatures and compositions. We begin by using density functional theory (DFT) to understand the nature of the interatomic interactions present in these two material systems. Next, using training sets composed of DFT results, we develop computationally inexpensive model Hamiltonians based on the cluster expansion method. Finally, we employ the Monte Carlo scheme to obtain thermally averaged ensemble size and shape distributions in the AuPd and AuPt surface alloys, which we present and explain in terms of interatomic interactions. By clarifying the connection between interatomic interactions and ensemble populations, we hope to offer guidance in the rational design of bimetallic catalyst materials.

II. Computational Methods

A. Density Functional Theory. Quantum mechanical calculations reported herein were performed on the basis of spin-polarized density functional theory within the generalized gradient approximation (GGA-PW91,²⁵ as implemented in the Vienna Ab-initio Simulation Package (VASP).²⁶ The projector augmented wave (PAW) method with a planewave basis set was employed to describe the interaction between ion cores and valence electrons. The PAW method is in principle an all-electron frozen-core approach that considers exact valence wave functions.²⁷ Valence configurations employed are 5d¹⁰6s¹ for

* To whom correspondence should be addressed. E-mail: gshwang@che.utexas.edu.

Au, $4d^95s^1$ for Pd, and $5d^96s^1$ for Pt. An energy cutoff of 350 eV was applied for the planewave expansion of the electronic eigenfunctions. To model the face-centered cubic (fcc) (111) surface, we used supercell slabs that consist of either a rectangular $2\sqrt{3} \times 4$ surface unit cell (for the results in Section III.A) or a hexagonal 4×4 surface unit cell (for the training sets described in Section II.B). Both shapes of cells include four atomic layers, each of which contains 16 atoms. The bottom three layers are pure Pd(111) or Pt(111) slabs, and the topmost is a monolayer alloy of the same species with Au. A slab is separated from its periodic images in the vertical direction by a vacuum space corresponding to seven atomic layers. The upper two layers of each slab were fully relaxed using the conjugate gradient method until residual forces on all the constituent atoms became smaller than 5×10^{-2} eV/Å, while the bottom two layers were fixed at corresponding Pd or Pt bulk positions. The lattice constants for bulk Pd, Pt, and Au are predicted to be 3.95, 3.98, and 4.18 Å, respectively, virtually identical to previous DFT-GGA calculations and also in good agreement with the experimental values of 3.89, 3.92, and 4.08 Å¹. For Brillouin zone integration, we used a $(2 \times 2 \times 1)$ Monkhorst–Pack mesh of k points to determine the optimal geometries and total energies reported in Section III.B. We increased the k -point mesh size up to $(7 \times 7 \times 1)$ to refine corresponding electronic structures reported in Section III.B and to $(4 \times 4 \times 1)$ to refine the total energies for use in the training sets in Section II.B. Previous calculations suggest that the chosen parameters are sufficient for describing the surface properties of the model systems considered.^{16,17}

B. Models for Alloy Surface Configurations.

B.1. Formulation of Cluster Expansions (CE). DFT is a well-established approach to study the structure and energetics of various materials. However, DFT calculations are computationally very expensive and even impractical for large systems containing more than a few hundred atoms, which are often needed for determining the configuration of multimetallic alloys. One means of extending the reach of DFT that has been used with great success is the cluster expansion (CE) method. A CE is a model Hamiltonian that is capable of reproducing DFT-predicted energies of binary crystalline alloys to within a few millielectronvolts per atom.^{28–34}

In the CE method, the occupation of lattice site i in a crystalline binary alloy of species A and B is represented by a pseudospin variable, s_i . Site i is assigned to be spin up ($s_i = +1$) if occupied by A and spin down ($s_i = -1$) if occupied by B. The initial assignment of spins to species is arbitrary. The total energy of a system with N lattice sites [$E(\hat{s})$, $\hat{s} = \{s_1, s_2, \dots, s_N\}$] is then expanded in terms of products of clusters of spins

$$E(\hat{s}) = J_0 + \sum_i J_i s_i + \sum_{i<j} J_{ij} s_i s_j + \sum_{i<j<k} J_{ijk} s_i s_j s_k + \dots \quad (1)$$

where J_0 , J_i , J_{ij} , and J_{ijk} are the interaction coefficients [called effective cluster interactions (ECIs)] for the empty, point, pair, and three body configurations. In this formulation, every cluster of sites explicitly possesses its own ECI. However, if the underlying symmetry of the lattice is respected, and all sites are considered equivalent, then clusters of sites that have the same shape must have equal ECIs. All first nearest neighbor pairs, for example, have the same ECI, while all second nearest neighbor pairs share a different ECI. Clusters of sites with a common shape are said to be of the same cluster-type. Using this definition, the spin products of all clusters of type t , which

contains M sites, can be averaged over the N sites of the lattice

$$\bar{C}_t(\hat{s}) = \frac{1}{N} \sum_{(i_1 < i_2 < \dots < i_M) \in t} s_{i_1} s_{i_2} \dots s_{i_M} \quad (2)$$

With the additional definition $\bar{C}_0(\hat{s}) = 1$ for the empty cluster, the CE can be rewritten as a sum over cluster-types

$$E(\hat{s}) = N \sum_t J_t \bar{C}_t(\hat{s}) \quad (3)$$

A complete CE contains every possible cluster-type. At least an equal number of independent data points derived from DFT or experimental results is necessary to uniquely determine the values of the corresponding ECIs. However, in practice, some clusters are more important than others, and a truncated CE can be constructed that provides an acceptable approximation of true energies.

B.2. Determination of CE Parameters. The fit of a truncated CE to a training set of DFT energies can be improved by adding more clusters. However, simply adding more clusters may carry the risk of overfitting, which degrades the ability of the CE to predict the energies of surfaces outside of the training set. Cross validation (CV) has been proposed to detect and prevent overfitting, while also providing a measure of the predictive ability of a CE model.³⁵ The optimal set of clusters with respect to a fixed training set of input data is obtained by minimizing the CV score (ξ), which is given by

$$\xi^2 = \frac{1}{N} \sum_{n=1}^N (E_{\text{DFT}}^{(n)} - E_{\text{CEM}}^{(n)})^2 \quad (4)$$

where $E_{\text{DFT}}^{(n)}$ is the DFT energy of the n th of N total surfaces in the training set, and $E_{\text{CEM}}^{(n)}$ is a prediction of the same energy by a CE with a particular set of clusters. The ECIs used in the calculation of $E_{\text{CEM}}^{(n)}$ are obtained by fitting to a subset of the full training set which excludes the n th slab, so that $E_{\text{DFT}}^{(n)} - E_{\text{CEM}}^{(n)}$ is a genuine prediction error. Consequently, the CV score of a truncated CE is a sum over N prediction errors obtained from N independent fittings of its associated ECIs.

We used simulated annealing (SA)³⁶ to determine the set of clusters that minimized the CV score. In this work, the fcc (111) surface was represented by a two-dimensional, hexagonal lattice with two types of 3-fold hollow sites. A hollow site is designated hexagonal close-packed (hcp) if an atom is present in the first subsurface layer directly beneath it and fcc if not. We considered all possible clusters in this representation of the surface that have a maximum width less than or equal to the third nearest neighbor distance. A total of 36 meet this criterion, including the empty and point clusters. The CE was encoded as a string of binary digits, with each bit indicating the inclusion of a particular cluster. The simulation was started from a string with only the empty, site, and pair interactions switched on. In every step, one bit was randomly selected and flipped. The CV score of the encoded CE was then computed. The new CE was kept with a probability equal to

$$P = \exp[-(\xi_{\text{new}} - \xi_{\text{old}})\beta] \quad (5)$$

where β is a fictitious inverse temperature. Over the duration of each SA run, β was slowly increased. At the start of these

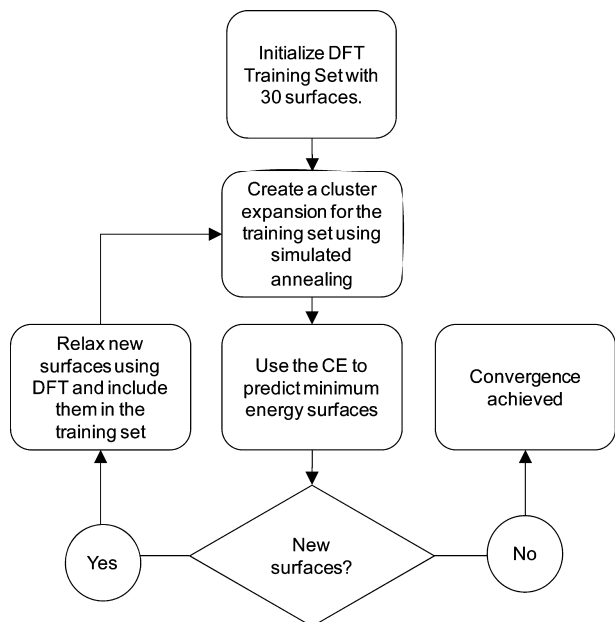


Figure 1. Flowchart of the algorithm used to create the cluster expansions. This procedure was followed once for AuPt/Pt(111) and once for AuPd/Pd(111).

simulations, when β is low (i.e., the temperature is high), the CV score surface can be freely explored. As β is increased, the simulation becomes trapped in a basin and funneled down to the minimum. To help ensure that a global minimum had been reached, all SA runs were repeated 12 times starting from different random seeds.

The final CEs were created using an iterative procedure^{35,37} as illustrated in Figure 1. The initial training sets for the AuPt and AuPd alloys each contained 30 model surfaces with every possible surface composition ($\text{Au}_{16-x}\text{Pt}_x/\text{Pd}_x$, where $x = 0, 1, \dots, 16$) represented at least once. From these, a trial CE for each alloy was constructed by using simulated annealing to minimize the CV score as described above. The trial CEs were used to predict minimum-energy surfaces for all compositions, which then were relaxed using DFT and added to their respective training set if not already present. The trial CE was considered to be fully converged if it predicted no new minimum-energy surfaces. Otherwise, the enlarged training set was used to generate a new trial CE, and the procedure was repeated. For the AuPd surface alloy, convergence was achieved after four iterations, during which 26 model surfaces were added to the training set. The AuPt surface alloy required five iterations and 21 additional model surfaces.

For comparison, CEs that included only up to first nearest neighbor (1NN) pair interactions also were created for each alloy, taking

$$E^{\text{1NN}}(\hat{s}) = J_0 + J_1 \sum_i s_i + J_{\text{1NN}} \sum_{i < j \in \text{1NN}} s_i s_j \quad (6)$$

where J_0 , J_1 , and J_{1NN} were fit to the training sets just described. Training set formation energies calculated using the 1NN CEs are compared to DFT in Figure 2 together with the longer-range, multisite (“3NN”) CEs. Accounting for multibody and longer range interactions reduces the mean error [$\bar{\epsilon}$ in Figure 2] of the AuPt CE by a factor of 9.8, and the AuPd CE by a factor of 4.2. The cluster-types and ECIs for the 3NN expansions are included in the Supporting Information.

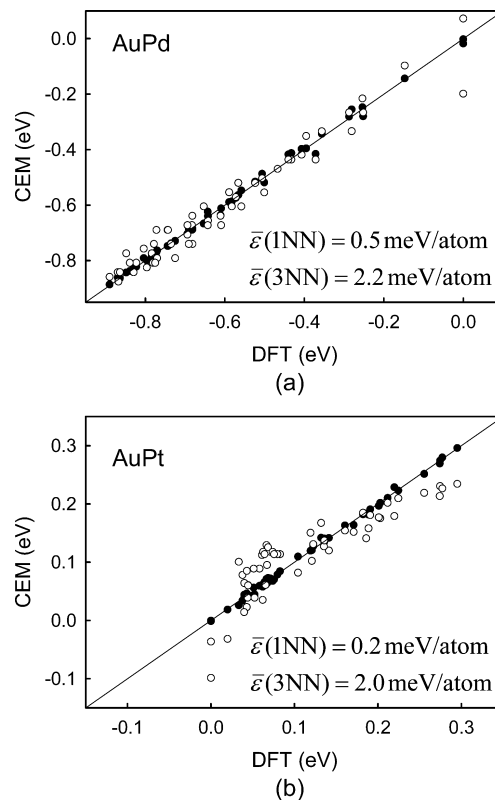


Figure 2. Parity plots showing discrepancies between CE and DFT predictions. Open circles are for 1NN models, and filled circles are for 3NN models. The mean errors, $\bar{\epsilon}(1\text{NN})$ and $\bar{\epsilon}(3\text{NN})$, are averages of the discrepancies over all N surfaces in the training sets, each of which has 16 surface atoms.

B.3. Monte Carlo (MC) Simulation. In the canonical (NVT) ensemble, the expectation value of a property $\langle A \rangle$ of a thermally equilibrated system can be calculated by³⁸

$$\langle A \rangle = \frac{\sum_i A_i e^{-E_i/k_B T}}{\sum_i e^{-E_i/k_B T}} \quad (7)$$

where the sums are over all microstates. While for many systems there is no obvious, tractable way to directly calculate $\langle A \rangle$ using this expression, a Monte Carlo algorithm can be used to obtain a reasonable estimate.³⁹ In general, the algorithm has four main steps as illustrated in Figure 3. First, the microstate from the previous (or initial) iteration is randomly changed to produce a new microstate. For this study, we swapped the spins of two randomly chosen lattice sites. Second, the energy of the new microstate is calculated. Third, the probability of transitioning to the new microstate is calculated using the Boltzmann factor. This probability is compared to a random number between 0 and 1. If the random number is smaller, transition is successful. The microstate from the previous iteration is discarded, and the new microstate is kept. Otherwise, the previous microstate is retained. During the fourth and final step before the beginning of the next iteration, the properties of the microstate are calculated and accumulated. After a preset number of iterations over these four steps, the collected data is arithmetically averaged to yield ensemble averages.

Using MC in the canonical (NVT) ensemble and CE Hamiltonians, we simulated AuPt and AuPd surface alloys with

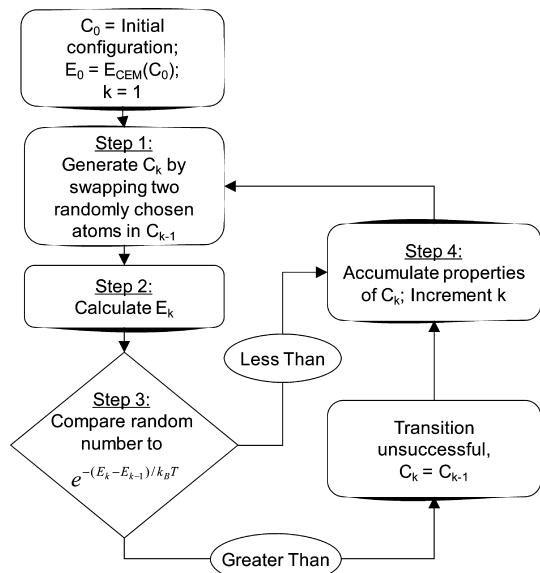
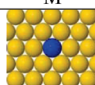
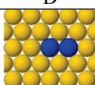
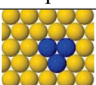


Figure 3. Monte Carlo algorithm. The iteration number is k , and the surface configurations and their energies are stored in C_k and E_k , respectively.

TABLE 1: Calculated Formation Energies (in eV) of Pd/Pt Ensembles^a

	M	D	T
			
AuPd	0.07	0.11	0.15
AuPt	0.25	0.24	0.23

^aThe blue and yellow represent the Pd/Pt and Au atoms, respectively.

a Pt/Pd coverage between 5 and 50% at temperatures between 100 and 800 K. All simulated surfaces were 30×30 hexagonal surface unit cells (= 900 surface atoms) in size and were terminated at their edges by periodic boundaries. To reduce the influence of the initial surface configurations on the final results, the simulations were all started at a high temperature of 1000 K, then cooled to the target simulation temperature over a period of 1.8×10^7 steps (2×10^4 steps per surface atom). Then, the surfaces were permitted to equilibrate at the target temperature for 4.5×10^7 steps (5×10^4 steps per surface atom). After the equilibration period, data collection began. The number, size, and shape of Pd/Pt ensembles in each sampled microstate were collected and averaged over 9×10^6 steps (10^4 steps per surface atom).

III. Results and Discussion

A. Stability of Small Pd/Pt Ensembles: DFT Calculations.

We first calculated and compared the formation energies of small, isolated Pd/Pt ensembles [i.e., monomer (M), dimer (D), and hcp trimer (T)] in the AuPd/Pd(111) and AuPt/Pt(111) surface alloys (see the illustrations above Table 1) to examine their relative stability. Here, the ensemble formation energy per X atom (E_f , X = Pd, Pt) is given by $E_f = \{E_{\text{AuX}} - E_{\text{Au}} + N_X(E_{\text{Au-bulk}} - E_{\text{X-bulk}})\}/N_X$, where E_{AuX} , E_{Au} , $E_{\text{Au-bulk}}$, and $E_{\text{X-bulk}}$ represent the total energies of AuX/X(111), Au/X(111), bulk Au (per atom), and bulk X (per atom), respectively, and N_X indicates the number of X atoms in the AuX surface alloy. As summarized in Table 1, predicted Pd monomer, dimer, trimer formation energies (per atom) are $E_f(\text{M}) = 0.07$ eV, $E_f(\text{D}) =$

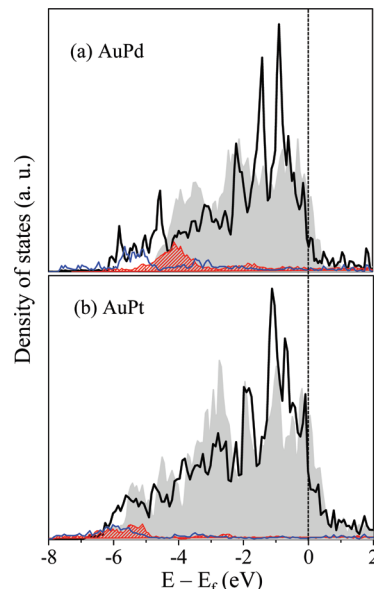


Figure 4. Density of states projected on the outmost s and d states of Pd/Pt monomer and pure Pd/Pt(111) surfaces. The s and d states are represented respectively by the shaded gray and patterned red areas in the monomer cases and by the thick black and thin blue solid lines in the pure surface cases. The vertical dotted line indicates the Fermi level position.

0.11 eV, and $E_f(\text{T}) = 0.15$ eV, respectively; taking these values, $\text{M} + \text{M} \rightarrow \text{D}$ and $\text{M} + \text{D} \rightarrow \text{T}$ agglomeration reactions tend to be endothermic by 0.08 eV [$\Delta E_{\text{D}} = 2E_f(\text{D}) - 2E_f(\text{M})$] and 0.16 eV [$\Delta E_{\text{T}} = 3 \times E_f(\text{T}) - 2E_f(\text{D}) - E_f(\text{M})$], respectively. This suggests that Pd would have a tendency to remain isolated, rather than forming aggregates in the AuPd surface alloy. In contrast, the corresponding agglomeration reactions for Pt turn out to be slightly exothermic, that is, $\Delta E_{\text{D}} = -0.02$ eV and $\Delta E_{\text{T}} = -0.05$ eV; implying that Pt may favor clustering.

Figure 4 shows the local density of states (LDOS) projected onto the d-bands of a Pd/Pt monomer in the AuPd/AuPt surface alloy; LDOS plots for pure Pd(111)/Pt(111) surfaces are also presented for comparison. The LDOS of the Pd monomer noticeably broadens as compared to the Pd(111) case; in particular, the onset of the high binding energy tail shifts down below -6 eV (from around -5 eV in Pd(111)) while the peaks near the Fermi level (-1 eV $< E - E_f$) appear to be reduced. On the other hand, the Pt monomer exhibits more pronounced LDOS peaks in the low binding energy region (-2 eV $< E - E_f$) at the cost of reduction in the higher binding energy peaks ($E - E_f < -2$ eV). As a result of these differences in the LDOS, the d-band centers for Pd and Pt monomers are shifted relative to the respective pure Pd and Pt surfaces. In the Pt case, the d-band center of the monomer is 0.09 eV higher than that of Pt(111). The shift is in the opposite direction for Pd; the monomer is 0.07 eV lower than Pd(111). These results suggest that, in AuPt surface alloys, the homonuclear Pt–Pt interaction would be energetically more favorable than the heteronuclear Pt–Au interaction, while in AuPd surface alloys, the heteronuclear Au–Pd interaction tends to be stronger. This opposite tendency in the interatomic interactions may result in markedly different atomic arrangements in AuPd and AuPt surface alloys, as discussed in the following sections.

B. Surface Atomic Arrangements: MC Simulations.

B.1. Ensemble Size Distributions. Using MC simulations, we first calculated the size distributions of ensembles on AuPd and AuPt alloy surfaces at $T = 300$ K and a Pd/Pt coverage of $\theta = 20$ at. %. Figure 5 shows how Pd and Pt are distributed into

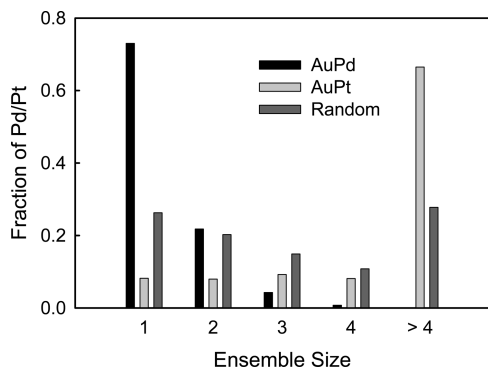


Figure 5. Ensemble size distribution at $T = 300$ K and $\theta = 20\%$. In the AuPd surface alloy (black bars, leftmost in each group), smaller ensembles are preferred. Larger ensembles are preferred in the AuPt surface alloy (light gray, center in each group). Results for the random alloy (dark gray, rightmost in each group) are included for comparison.

small ensembles of size $N = 1-4$, and also the fractions of each which exist in larger islands containing more than four contiguous atoms. For comparison, predictions made using a random alloy of noninteracting spins are also included. In AuPd, most of the Pd atoms, around 73%, exist as monomers. This is about 2.8 times larger than predicted by the random model. As N increases, the Pd fraction decreases sharply, becoming comparable to the random alloy for $N = 2$, but almost vanishing for $N > 4$. Relative to the random model, the formation of small ensembles is clearly preferred on the AuPd surface. This is consistent with the energetic favorability of Au–Pd interactions relative to Pd–Pd; as ensembles become larger, the number of Au neighbors per Pd atom tends to decrease. In AuPt, where the reverse relationship holds, our calculations show a preference for larger ensembles. The majority of Pt atoms, about 67%, are part of ensembles with $N > 4$. This is about 2.4 times larger than the fraction predicted by the random model. For smaller ensembles with $N = 1$ to $N = 4$, the Pt fraction is less than the random prediction.

Figures 6 and 7 show the effects of temperature and coverage on monomer and dimer populations in AuPd and AuPt surface alloys. Behavior in the high (“infinite”) temperature limit, where atomic interactions are negligible, can be represented by the random alloy. Results for the random alloy are also a helpful reference for explaining and comparing the finite temperature behavior of the two alloys, and so are presented alongside the finite temperature results in both Figures 6 and 7. Although the infinite temperature results presented in Figures 6 and 7 are identical, for clarity, we will refer only to the AuPd surface alloy (Figure 6a,b) in our description of them.

At infinite temperature, the fraction of surface Pd atoms that exist as monomers (Figure 6a) monotonically decreases with increasing coverage. This is a consequence of the fact that when the surface contains few Pd atoms, the probability of finding two or more together is low, but as the surface becomes more crowded, it increases. Unlike the monomer plot, the infinite temperature dimer plot (Figure 6b) passes through a maximum at approximately $\theta = 12\%$. As more Pd atoms crowd the surface, the probability of randomly placing two together increases. This explains the initial rise. However, the same is true of trimers, tetramers, and other, larger ensembles. The fraction of Pd atoms in dimers must at some point give way to the growing fraction in larger ensembles and begin to diminish.

The overall shape of most of the finite temperature Pd monomer plots (Figure 6a) resembles the infinite temperature

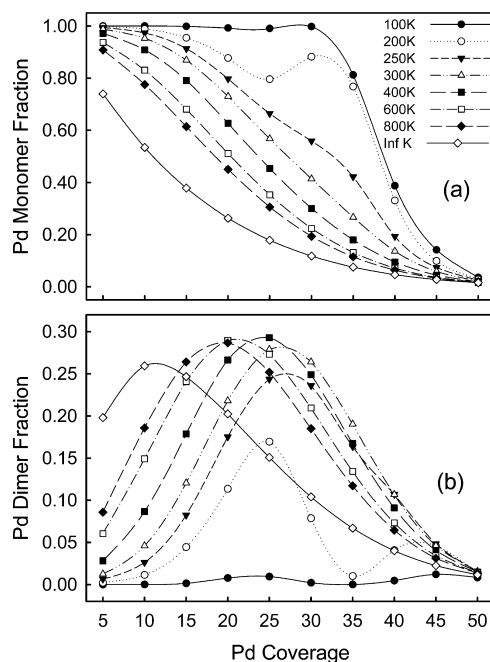


Figure 6. Average fraction of surface Pd atoms in monomers (a) and dimers (b) in AuPd surface alloys at several levels of coverage and temperature. As temperature increases, the monomer population declines, and the peak in the dimer population shifts toward higher coverage.

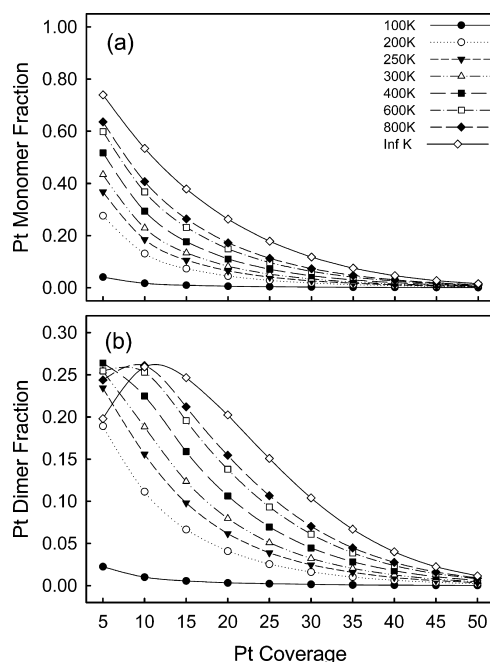


Figure 7. Average fraction of surface Pt atoms in monomers (a) and dimers (b) in AuPt surface alloys at several levels of coverage and temperature. As temperature increases, the monomer population also increases, and the peak in the dimer population shifts toward lower coverage.

limit. The $T = 100$ and 200 K plots are exceptions. The maxima they exhibit at $\theta = 30-35\%$ can be attributed to the stability of the $(\sqrt{3} \times \sqrt{3})R30^\circ$ ordered phase,²² as will be explained in greater detail below. Regardless of temperature, at $\theta = 5\%$, between 74 and 100% of Pd atoms are monomers, but at $\theta = 50\%$, fewer than 4% are. As expected, reducing the temperature (thereby increasing the contribution of interatomic interactions) results in a significant enhancement of the monomer population at all levels of coverage. At $\theta = 30\%$ and $T = 100$ K, close to

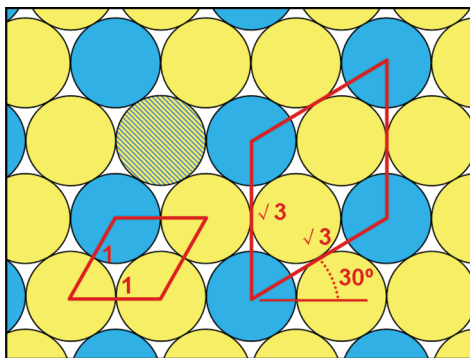


Figure 8. The $(\sqrt{3} \times \sqrt{3})R30^\circ$ ordered surface. Yellow atoms are Au and blue atoms are Pd. The polygon on the left shows the unit cell for the hexagonal lattice with unit length basis vectors. The polygon on the right shows the unit cell for the ordered surface. The striped atom is Au in the perfectly ordered surface. If it is swapped with one of the three adjacent Pd atoms, a Pd trimer is formed. A Pd tetramer is formed if it is swapped with any nonadjacent Pd atom.

100% of Pd atoms exist as monomers, while at $T = \infty$, only around 12% do. Even at 800 K, the monomer fraction differs from the random model by as much as 24 percentage points (at $\theta = 10\%$).

Plots of the Pd dimer fractions (Figure 6b) at the finite temperatures considered exhibit maxima, just as at infinite temperature. However, relative to the random alloy, the maxima are shifted increasingly toward higher coverage as temperature decreases. The shift is equal to about 15 percentage points in the $T = 250$ K case. This is apparently due to the preference for small ensembles in the AuPd surface alloy. The preference for monomers over dimers delays the rise of the dimer fraction and decline of the dimer fraction likewise is delayed by the preference for dimers over larger ensembles.

The $T = 100$ and 200 K dimer plots have minima at $\theta = 30\text{--}35\%$ that coincide with the previously mentioned maxima in the monomer plots. These features in the low-temperature dimer and monomer plots can be explained by the stability of the ordered $(\sqrt{3} \times \sqrt{3})R30^\circ$ surface, which can form at a Pd coverage of exactly one-third. As illustrated in Figure 8, every Pd atom is surrounded by six Au nearest neighbors and six Pd second nearest neighbors. The surface is unique in that (i) it is the only one with a coverage of one-third in which all Pd atoms can exist as monomers; and (ii) no such surfaces exist at Pd coverage $> 1/3$. The CE predicts the $(\sqrt{3} \times \sqrt{3})R30^\circ$ phase to be the ground state for the Au_2Pd surface. Moreover, swapping any pair of dissimilar atoms creates either a Pd trimer, which incurs an energy penalty of 0.12 eV, or a tetramer, with a penalty of 0.18 eV. These energy penalties are not trivial, particularly at low temperatures. In the MC scheme, the probability of transitioning from the ground state to a microstate containing a single trimer at $T = 200$ K is $\exp(-0.12 \text{ eV}/k_B T) = 9.5 \times 10^{-4}$. This explains the strong preference for monomers and near absence of dimers on low-temperature AuPd surfaces with $\theta \approx 1/3$.

In the AuPt surface alloy, the effects of temperature on the populations of monomers and dimers are all the opposite of those for AuPd, due to the energetic favorability of Pt–Pt interactions over Au–Pt. Monomer populations (Figure 7a) decrease with temperature for all levels of coverage. At $T = 100$ K and $\theta = 5\%$, about 4% of surface Pt exists as monomers, compared to 74% in the random alloy. Even at 300 K, the fraction rises to only about 43%. Maxima in the AuPt dimer plots (Figure 7b) are clearly visible only in the 600 and 800 K

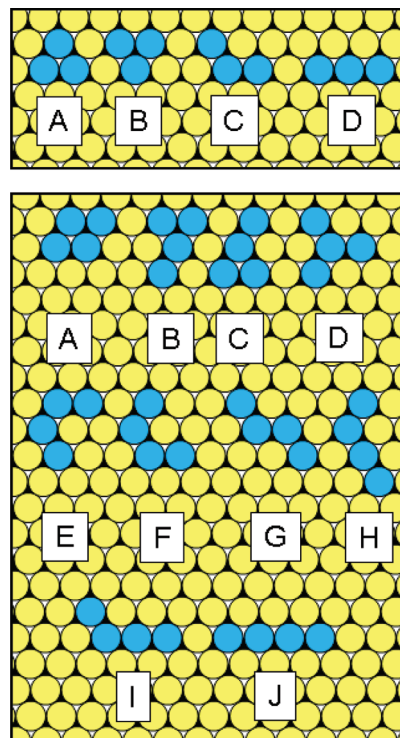


Figure 9. The 4 types of contiguous trimers (upper panel) and 10 types of contiguous tetramers (lower panel) in the fcc (111) surface, accounting for the two types of 3-fold hollow sites. Black interstitial fill marks the presence of an atom in the first subsurface layer.

trends. They have been shifted as in the AuPd surface, but toward lower, rather than higher, coverage.

B.2. Shape Distributions of Trimers and Tetramers. Finally, we examined the shapes of ensembles in AuPt, AuPd, and random surface alloys. Here, only trimers and tetramers are considered. Four shapes of trimers and ten shapes of tetramers are possible in the fcc (111) surface. They are shown schematically in Figure 9. The order of their labeling (A–D for trimers and A–J for tetramers) corresponds to their spatial extent in the surface.

Figure 10 shows the predicted shape distributions of trimers and tetramers in a surface with $\theta = 30\%$ at $T = 300$ K. In the random alloy, around 12% of trimers are compact-fcc (Shape A), 12% are compact-hcp (B), 51% are bent-linear (C), and 25% are linear (D). These fractions differ from one another despite there being no difference in the formation energies of the four shapes. This can be understood by recognizing that if the total number of orientations of each shape is counted separately, there are actually 11 possible trimers in the surface, rather than 4. The two compact shapes account for one each, the bent-linear shape accounts for six, and the linear shape accounts for three, as shown in Figure 11. Each of the 11 total orientations is equally probable, so the compact-hcp and compact-fcc shapes each account for $1/11$ ($= 9.1\%$) of the total number of trimers, bent-linear for $6/11$ ($= 54.5\%$), and linear for $3/11$ ($= 27.3\%$). These fractions differ somewhat from the ones obtained via MC simulation and reported in Figure 10. The discrepancies appear to be an effect of coverage. In the low coverage limit, our simulations show that the MC results approach the fractions just calculated, but as coverage increases the compact trimer fraction rises at the expense of the bent-linear and linear fractions. All of the foregoing applies in a similar way to tetramers. Further details will be presented elsewhere.

The AuPt and AuPd shape distributions differ a great deal from one another and from the random alloy results. The

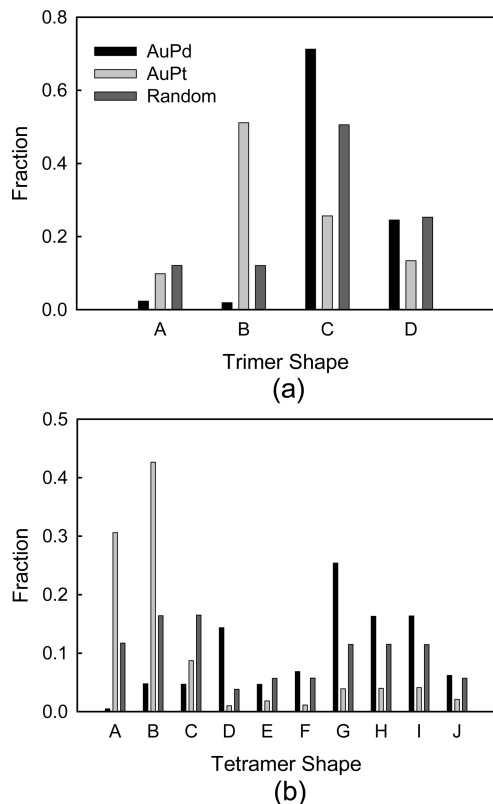


Figure 10. Trimer and tetramer shape distributions at $T = 300$ K and $\theta = 30\%$. More compact trimers (those with more homonuclear interactions) are favored in the AuPt (light gray, center bars) surface, and more extended trimers (with more heteronuclear interactions) are favored in AuPd (black, leftmost bars).

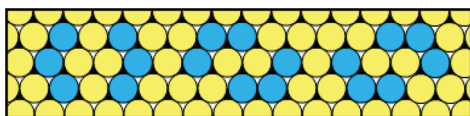


Figure 11. Every trimer and tetramer shape possesses one or more orientations. The six possible orientations of the bent trimer (trimer shape C) are shown here for illustration.

fractions of Pd trimers (Figure 10a) that adopt the compact-fcc and compact-hcp shapes are smaller than the random model predictions by factors of 5.2 and 6.4, respectively. The compact-fcc and -hcp trimer fractions are much larger in the AuPt case than in AuPd, around 0.8 and 4.2 times the size of the random prediction. Here, we note that the large difference between the populations of fcc and hcp compact trimers (shapes A and B) in AuPt is due to the difference in their formation energies. These two types of trimers are identical in terms of the numbers of Pt–Pt, Au–Pt, and Au–Au pair interactions associated with them, which indicates that a Hamiltonian must include multisite interactions to distinguish between them. For the bent-linear trimer shape, the Pd fraction is about 1.4 times larger than the random prediction, while the Pt fraction is smaller by about half. The Pd fractions for the compact tetramer shapes A, B, and C are all much smaller than the prediction for either AuPt or the random alloy, but as can be seen in Figure 10b, the fractions for the more extended tetramers D–I are comparatively larger. Conversely, in the AuPt alloy, relatively few tetramers have the extended shapes (D–I), but a large fraction are compact (A–C).

The differences in the AuPd and AuPt shape distributions can once again be explained by interatomic interactions. Compact ensembles contain a larger number of homonuclear,

nearest-neighbor interactions than extended ones. The compact trimers contain three such interactions, while the bent-linear and linear each contain two. The most compact tetramer shape (A) contains five, tetramers B and C contain four, and the remainder each contain three. Accordingly, in the AuPd alloy, where heteronuclear interactions are favored over homonuclear, the fraction of trimers and tetramers that have compact shapes is smaller than in the AuPt alloy. The opposite is true of the more extended shapes, which are more likely to be found in AuPt.

IV. Summary

Using the cluster expansion method, model Hamiltonians were constructed for AuPt/Pt(111) and AuPd/Pd(111) surface alloys. These cluster expansions match DFT-calculated energies to within a fraction of an millielectronvolts per surface atom. They are also sufficiently computationally inexpensive to enable their use in MC simulations. We used the MC scheme to predict the size and shape distributions of Pd and Pt surface ensembles for a range of compositions and temperatures. The results of the MC simulations show that the surface ensemble populations are strongly influenced by the interatomic interactions present in AuPt/Pt(111) and AuPd/Pd(111) surface alloys. The origin of these interactions is revealed by DFT predictions of the formation energies and electronic structures of small Pt and Pd ensembles in model alloys, which show that homonuclear (Pt–Pt) interactions are favored in AuPt surface alloys, while heteronuclear (Au–Pd) are favored in AuPd. As a consequence, AuPd exhibits a strong preference for small ensembles compared to the AuPt alloy and a random alloy (with no interactions), according to our MC simulations. For example, at 300 K and 20% coverage, 73% of surface Pd atoms are monomers. The corresponding quantities in the AuPt and random alloys are predicted to be 26 and 8%, respectively. Similarly, at this level of coverage and temperature, a negligible fraction of surface Pd belongs to ensembles that contain five or more contiguous atoms, but around 67% of surface Pt is part of ensembles of this size. The differences in interatomic interactions also explain the influence of coverage and temperature on monomer and dimer populations in the two alloys. Monomer populations in AuPd are seen to increase as temperature is reduced, while the reverse happens in AuPt. Maxima in the dimer populations are also shifted in opposite directions as temperature increases, toward higher coverage in AuPt and toward lower in AuPd. Our MC simulations also demonstrate that compact ensembles that contain a greater number of homonuclear interactions are favored in AuPt, while more extended shapes are preferred in AuPd. The computational scheme described here can be extended to evaluate a host of other potential influences on ensemble formation in bimetallic surfaces, such as their crystallographic orientation, degree of strain, the presence of adsorbates, interactions with the catalyst support, and their bulk composition.

Acknowledgment. We acknowledge the Robert A. Welch Foundation (F-1535) and the National Science Foundation (NSF-IGERT Grant DGE-0549417) for the support of this work. All our calculations were performed using supercomputers in Texas Advanced Computing Center at the University of Texas at Austin.

Supporting Information Available: The cluster expansions for the AuPd/Pd(111) and AuPt/Pt(111) surface alloys are listed. This material is available free of charge via the Internet at <http://pubs.acs.org>.

References and Notes

- (1) Campbell, C. T. *Annu. Rev. Phys. Chem.* **1990**, *41*, 775.
- (2) Rodriguez, J. A.; Goodman, D. W. *J. Phys. Chem.* **1991**, *95*, 4196.
- (3) Rodriguez, J. A. *Surf. Sci. Rep.* **1996**, *24*, 223.
- (4) Chen, M. S.; Kumar, D.; Yi, C. W.; Goodman, D. W. *Science* **2005**, *310*, 291.
- (5) Mott, D.; Luo, J.; Smith, A.; Njoki, P. N.; Wang, L.; Zhong, C.-J. *Nano. Res. Lett.* **2007**, *2*, 12.
- (6) Gao, F.; Wang, Y.; Goodman, D. W. *J. Am. Chem. Soc.* **2009**, *131*, 5734.
- (7) Sachtler, J. W. A.; Somorjai, G. A. *J. Catal.* **1983**, *81*, 77.
- (8) Edwards, J. K.; Carley, A. F.; Herzing, A. A.; Kiely, C. J.; Hutchings, G. J. *Faraday Discuss.* **2008**, *138*, 225.
- (9) Allison, E. G.; Bond, G. C. *Catal. Rev.* **1972**, *7*, 233.
- (10) Pluntke, Y.; Kibler, L. A.; Kolb, D. M. *Phys. Chem. Chem. Phys.* **2008**, *10*, 3684.
- (11) Park, J. B.; Conner, S. F.; Chen, D. A. *J. Phys. Chem. C* **2008**, *112*, 5490.
- (12) Liu, P.; Nørskov, J. K. *Phys. Chem. Chem. Phys.* **2001**, *3*, 3814.
- (13) Groß, A. *Top. Catal.* **2006**, *37*, 29.
- (14) Burch, R. *Acc. Chem. Res.* **1982**, *15*, 24.
- (15) Baddeley, C. J.; Tikhov, M.; Hardacre, C.; Lomas, J. R.; Lambert, R. M. *J. Phys. Chem.* **1996**, *100*, 2189.
- (16) Ham, H. C.; Hwang, G. S.; Han, J.; Nam, S. W.; Lim, T. H. *J. Phys. Chem. C* **2009**, *113*, 12943.
- (17) Ham, H. C.; Hwang, G. S.; Han, J.; Nam, S. W.; Lim, T. H. *J. Phys. Chem. C* **2010**, *114*, 7.
- (18) Pandelov, S.; Stimming, U. *Electrochim. Acta* **2007**, *52*, 5548.
- (19) Maroun, F.; Ozanam, F.; Magnussen, O. M.; Behm, R. *J. Science* **2001**, *293*, 1811.
- (20) Gao, F.; Wang, Y. L.; Goodman, D. W. *J. Am. Chem. Soc.* **2009**, *131*, 5734.
- (21) Zhang, J.; Jin, H. M.; Sullivan, M. B.; Chiang, F.; Lim, H.; Wu, P. *Phys. Chem. Chem. Phys.* **2009**, *11*, 1441.
- (22) Boscoboinik, J. A.; Plaisance, C.; Neurock, M.; Tysoe, W. T. *Phys. Rev. B* **2008**, *77*, 045422.
- (23) Boscoboinik, J. A.; Calaza, F. C.; Gavey, M. T.; Tysoe, W. T. *J. Phys. Chem. C* **2010**, *114*, 1875.
- (24) Bergbreiter, A.; Alves, O. B.; Hoster, H. E. *Chem. Phys. Chem.* **2010**, *11*, 1505.
- (25) Perdew, J. P.; Wang, Y. *Phys. Rev. B* **1992**, *45*, 13244.
- (26) Kresse, G.; Furthmüller, J. *VASP the Guide*; Vienna University of Technology: Vienna, Austria, 2001.
- (27) Blöchl, P. E. *Phys. Rev. B* **1994**, *50*, 17953.
- (28) Connolly, J.; Williams, A. *Phys. Rev. B* **1983**, *27*, 5169.
- (29) Ferreira, L.; Wei, S.; Zunger, A. *Phys. Rev. B* **1989**, *40*, 3197.
- (30) Laks, D. B.; Ferreira, L.; Froyen, S.; Zunger, A. *Phys. Rev. B* **1992**, *46*, 12587.
- (31) Blum, V.; Zunger, A. *Phys. Rev. B* **2004**, *70*, 155108.
- (32) Blum, V.; Zunger, A. *Phys. Rev. B* **2004**, *69*, 020103.
- (33) Barabash, S. V.; Blum, V.; Müller, S.; Zunger, A. *Phys. Rev. B* **2006**, *74*, 035108.
- (34) Yuge, K.; Seko, A.; Kuwabara, A.; Oba, F.; Tanaka, I. *Phys. Rev. B* **2007**, *76*, 045407.
- (35) van De Walle, A.; Ceder, G. *J. Phase Equilib.* **2002**, *23*, 348.
- (36) Quinn, M. J. *Parallel Programming in C with MPI and OpenMP*; Tata McGraw-Hill: New Dehli, 2004.
- (37) Zunger, A.; Wang, L. G.; Hart, G. L.; Sanati, M. *Modell. Simul. Mater. Sci. Eng.* **2002**, *10*, 685.
- (38) Hill, T. *An Introduction to Statistical Thermodynamics*; Dover Publications: New York, 1986.
- (39) Frenkel, D.; Smit, B. *Understanding Molecular Simulation: From Algorithms to Applications*; Academic Press: San Diego, 1996.

JP1074384